Rapid analysis of cell-generated forces within a multicellular aggregate using microsphere-based traction force microscopy

Journal:	*Soft Matter*
Manuscript ID	SM-ART-12-2019-002377.R1
Article Type:	Paper
Date Submitted by the Author:	02-Mar-2020
Complete List of Authors:	Kaytanli, Bugra; University of California Santa Barbara, Mechanical Engineering Khankhel, Aimal; University of California Santa Barbara, Biomolecular Science and Engineering Cohen, Noy; Technion Israel Institute of Technology, Materials Science Valentine, Megan; University of California Santa Barbara, Mechanical Engineering

Rapid analysis of cell-generated forces within a multicellular aggregate using microsphere-based traction force microscopy

Buğra Kaytanlı[a]*, Aimal H. Khankhel[b]*, Noy Cohen[c]†, Megan T. Valentine[a]†

[a]Department of Mechanical Engineering, University of California, Santa Barbara, CA 93106, U.S.A.
[b]Biomolecular Science and Engineering Program, University of California, Santa Barbara, CA 93106, U.S.A.
[c]Department of Materials Science and Engineering, Technion – Israel Institute of Technology, Haifa 3200003, Israel

We present a new approach to measuring cell-generated forces from the deformations of elastic microspheres embedded within multicellular aggregates. By directly fitting the measured sensor deformation to an analytical model based on experimental observations and invoking linear elasticity, we dramatically reduce the computational complexity of the problem, and directly obtain the full 3D mapping of surface stresses. Our approach imparts extraordinary computational efficiency, allowing tractions to be estimated within minutes and enabling rapid analysis of microsphere-based traction force microscopy data.

1 Introduction

Cells mechanically interact with their external microenvironment by applying tractions to their surroundings [1, 2]. These cell-generated boundary forces regulate critical cell functions including transcription, differentiation and proliferation [3-6], and measuring such forces in native three-dimensional (3D) cellular microenvironments is critical to understanding the interplay of mechanical and intercellular events.

Several strategies to measure the 3D deformations of solid but compressible hydrogel microspheres have been reported [7-10]. We refer to these as microsphere-based traction force microscopy (μTFM) methods. Unlike encapsulation of isolated single cells within 3D elastic matrices [11-13], in μTFM, microspheres are located between cells, maintaining native cell-cell contacts and allowing forces to be measured within a tissue. In contrast to liquid oil droplet sensors [14, 15], cells can exert both shear and normal tractions on the microsphere surface and can report isotropic loading. However, the computational requirements of finite element (FE) analysis of the traction fields has limited progress [9, 11] and forced simplifications, such as reporting only compressional stress determined from sensor volume changes under cell loading [7, 8], assuming uniform loading profiles within the tissue [10], or using the microspheres to introduce compliant surfaces without measuring cell-generated forces [16].

Here, we present an improved approach to μTFM, in which we determine the tractions cells exert on compressible hydrogel microsensors by directly fitting their boundary displacements to an analytical solution of linear elasticity, thus avoiding FE approaches altogether. Our method imparts extraordinary computational efficiency, allowing tractions to be estimated within minutes and enabling rapid analysis of microsphere-based traction force microscopy data. This method is particularly useful for measuring the tractions developed within multicellular aggregates or tissue fragments, which are not accessible with standard TFM approaches.

2 Results and Discussion

2.1 Synthesis and Characterization of the Microsphere Sensors

Experimentally, elastic and compressible hydrogel microspheres were formed, functionalized to promote cell attachment, equilibrated with media, mixed with cells and returned to culture, where the cells can then exert both shear and normal tractions on the microsphere surface (Fig. 1 a-c; see Note 1, Supplemental Materials for full experimental details). We used biocompatible, UV-curable poly(ethylene glycol)-diacrylate (PEGDA), which has robust and tunable mechanical properties and a large linear elastic regime. In contrast to polyacrylamide [7, 8, 10, 17] and alginate [9], a wide range of commercially-available polymer architectures and functionalities are available to promote cell adherence and visualization [18, 19]. Additionally, PEGDA is mechanically stable and relative insensitive to solvent parameters. Unlike many swollen hydrogels formed from polyelectrolytes, PEGDA is non-ionic, so changes in pH and ionic strength have a modest effect on gel properties [20]. In this work, we maintain physiological osmolarity (~ 300 mOsm/kg) and pH (~7.4) conditions by pre-equilibrating the sensors with buffer or cell media and maintaining constant solvent conditions throughout the experiment.

Stiffness tunability can be achieved by changing the weight-fraction of the PEG backbone and/or the number of active acrylate groups. In this study all microspheres were synthesized with weight fractions of 4% PEGDA and fixed crosslinker density. The hydrogel stiffness sets the dynamic range of the sensor and influences the computational complexity: soft sensors may deform beyond the linear regime while the deformations of stiff sensors may not be detected. Additionally, since cells can sense and respond to the mechanics of substrates with which they interact, stiffness control allows for investigation of the interplay of cellular sensing, actuation, and function with μTFM [16].

To form the microspheres, a polydisperse water-in-oil emulsion was generated by mixing a solution containing an aqueous gel pre-cursor phase with non-ionic surfactants in a continuous phase of food-grade oil. The gel precursor contained PEGDA monomers (M_n=700 g/mol), a UV-excitable photoinitiator, and a small amount of both rhodamine-acrylate, to enable visualization and high-resolution shape determination of the microspheres via microscopy, and biotin-poly(ethylene glycol)-acrylate, to enable functionalization with cell adhesion molecules. Water-in-oil microdroplets were formed by emulsifying the solution by strong vortexing for several seconds. The high surface-tension between oil and water ensures that the unloaded microdroplets are perfectly round, and their size can be tuned by varying the surfactant composition or vortex intensity. These were immediately cured by photopolymerization to generate uniform isotropic elastic microspheres (Fig. 1a). After curing, the microspheres were rinsed several times with deionized water via centrifugation and resuspension to remove oil and unreacted materials. The resulting microspheres were functionalized with Neutravidin, washed, resuspended in a solution of the desired biotinylated adhesion molecule, then stored in cell culture media for use within 2 days.

The mechanical properties of the sensors were assessed experimentally. First, we confirmed that macroscopic gels fabricated under identical conditions responded linearly to applied shear strains of at least 10% with shear modulus $G' = 235 \pm 34$ Pa (Fig. 1d). Measurements were performed on an ARES-LS1 (TA Instruments) shear rheometer in a parallel-plate geometry with a 4-mm gap. Macroscopic
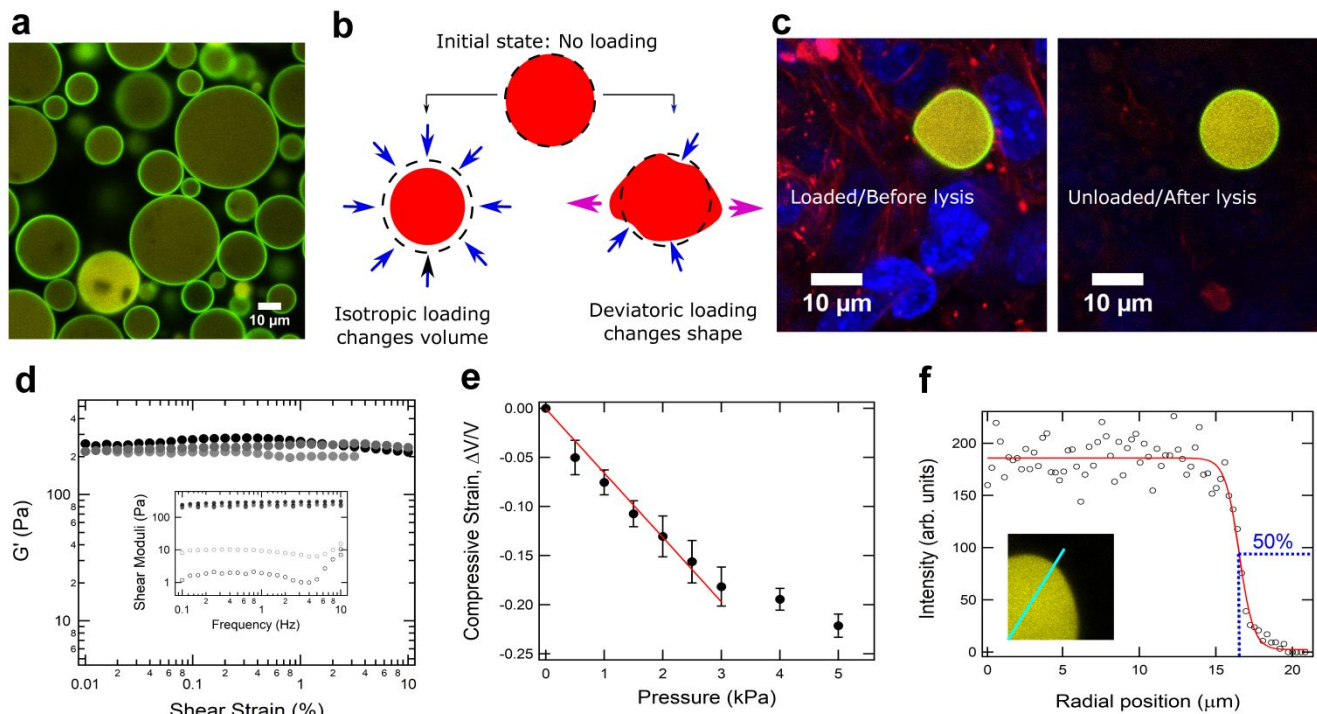
Figure 1. (a) Image of uniform, polydisperse microspheres after curing, **(b)** Schematic showing microsphere sensor deformation under isotropic and deviatoric loading. **(c)** Exemplar images of force sensors (blue, cell nuclei; red, F-actin; yellow, sensor volume; green, sensor surface) under cell loading (left) or after cell lysis (right). **(d)** The shear elastic modulus G' of a 4% PEGDA gel is independent of strain for strains up to 10%. **Inset**: The oscillatory shear data confirms that the hydrogel is elastic, with G' showing no significant dependence on frequency and $G' \gg G''$ for all frequencies measured. **(e)** The microsphere compression modulus is determined from sphere volume changes induced by an applied osmotic pressure. We find a linear elastic response to compression for strains up to ~ 15%. **(f)** Example of surface determination. The intensity profile (black circles) as a function of distance along a ray (shown in cyan) drawn through the fluorescently-labeled sensor body (inset). Sigmoidal fit (red) is used to determine the position of the surface (blue dotted line). Here, the surface is located at 16.52 ± 0.07 μm.

hydrogel materials ($n = 5$) were cast in a mold, photocured for 1 hour, and soaked in a 1X PBS bath overnight to allow them to equilibrate. To prevent slippage at the tool-hydrogel interface, tool surfaces were coated in 150 grit sandpaper and hydrogels were lightly superglued to sandpaper surfaces. To ensure uniform adhesion between the tool and hydrogel, the instrument head was slowly lowered until ~50 mN of axial force was achieved, and glue was allowed to cure for several minutes. The instrument head was then raised until the axial force was approximately 0 mN. Samples were trimmed to the plate size with a razor blade and all exposed edges were coated with silicone oil to prevent solvent evaporation during testing. Oscillatory strain sweep measurements were performed in the range of 0.01-10% to confirm that the hydrogel responded as a linear elastic solid in that regime (Fig. 1d). This is consistent with prior results demonstrating that similar PEGDA gels were linear in response to applied shear strains up to 40% [11]. The frequency-dependent storage (elastic) and loss (viscous) shear moduli, G' and G'', respectively, were measured using oscillatory shear-loading at frequencies ranging from 0.1-10 Hz at 1% strain, which was well within the linear shear loading regime (Fig. 1d, inset). To confirm that the hydrogels were fully crosslinked, we doubled the curing time ($n = 3$) and repeated the oscillatory shear frequency sweep

measurement: no significant change in mechanics was observed.

We independently measured the inverse of the osmotic compressibility (*e.g.* the bulk modulus) of the microspheres, *K*, by measuring the change in volume under isotropic osmotic compression [7, 21, 22] and found $K = 15.2 \pm 0.8$ kPa with a linear response to compressive strains of at least 15% (Fig. 1e, see Supplemental Materials). Experimentally, microspheres were synthesized as described and coated with a biotinylated poly-L-lysine and equilibrated with 1X phosphate buffered saline. Dilute solutions of microspheres were seeded into custom-made cover-glass bottomed wells and allowed to adhere. An osmotic stress was externally applied by the addition of a solution containing fluorescein-labeled, high molecular-weight (HMW) dextran (M_w=500 kD). The applied pressure was dependent on the concentration of dextran as previously reported [22]. Here, we achieved a pressure range of ~0 − 3 kPa using dextran concentrations ranging from ~20-45 µM. Imaging of the fluorescent HMW dextran confirmed that no dextran penetrated microspheres. In general, we would expect that fluid could drain from the swollen hydrogel as it is compressed leading to poroelastic effects and requiring corrections to the measured modulus; however, the microscale nature of the gel sensors we use enables rapid equilibration on times scales of < 1 sec so these effects can be ignored in our analysis [23]. Consistent with this, we see almost immediate equilibration of particle size upon solution exchange in our osmotic compression studies. We conservatively wait 5 minutes after solution exchange before imaging the particle volumes. After this equilibration time, volumetric images of microspheres were obtained using a Leica SP8 confocal microscope and volume-change ΔV was determined using ImageJ by measuring the change in microsphere radius *R* from the difference in maximum-intensity projections before and after solution exchange. The bulk modulus was determined from a linear fit of the data, which is plotted as applied osmotic pressure versus average volumetric compressive strain $\Delta V/V_0$, where V_0 is the initial sphere volume in the absence of dextran (as shown in Fig. 1e; *n*=15, 3 experiments). The measured mechanical properties can also be used to calculate the Poisson ratio $\nu = \frac{3K - 2G'}{2(3K + G')} \approx 0.49$.

2.2 Imaging and Surface Reconstruction

Each fluorescently labeled microsphere was imaged with a laser scanning confocal microscope before and after lysis to determine its loaded and traction-free shape, respectively (Fig. 1b, See Supplemental Materials for imaging conditions and details). Two sensor surface coatings were tested: poly-L-lysine (PLL) and RGD, which engage nonspecific electrostatic or ligand-specific integrin-based binding pathways, respectively. Hydrogel sensors are mixed with a solution of suspended mouse 3T3 fibroblast cells and immediately seeded onto PLL-coated glass-bottomed microwells (see Supplemental Materials for cell culture conditions). We found that cells with either coating robustly adhered to and deformed the microspheres. Each sensor acts as a 3D spring, changing its shape and size to achieve local force balance with the surrounding cells. Typically, each sensor is completely surrounded by cells (Fig. 1b).

Post-collection, the images were cropped for analysis of the surface of one microsphere. To approximate the point mapping along the surface of the sensor, we generated a unit vector array with the desired number of 'rays'. We typically used 2000 vectors, which were nearly uniformly distributed on the unit sphere. We placed the center of the resultant unit sphere at the calculated center of mass of the hydrogel microsphere, and then determined the 1D intensity of the image along the direction of each ray. Subsequently, the rays were rescaled such that the physical length of the ray was twice that of the approximated radius of the microsphere. To reduce the computation time and accommodate the differences in point spacing between the lateral (*x*, *y*) and axial (*z*) dimensions, we used a linear

interpolation method that determined the intensity along 100 points for each ray. We find our results to be fairly insensitive to the choice of length or number of points within the ray.

Next, the resultant intensity profile was fitted to a sigmoidal function, which is a good approximation of the typical signals we measure from the uniformly-labeled fluorescent microspheres (Fig. 1f). This approach assumes that each ray pierces the microsphere surface only once and that the ray passes through the surface reasonably close to normal, conditions easily met even for our most deformed microspheres. From the fit, and using the known coordinates of the projected vectors, we calculated the location of the surface. This was repeated for all surface points, resulting in a discretized boundary of the sensor in the unloaded and the loaded states (Fig. 2). The error in surface localization is approximately 100 nm. The use of boundary tracking enables efficient image processing, particularly for sensors subjected primarily to hydrostatic (normal) loading, as shown here, and reduces the effects of depth-dependent signal-to-noise degradation and light scattering from inhomogeneities within the extracellular matrix or cells.
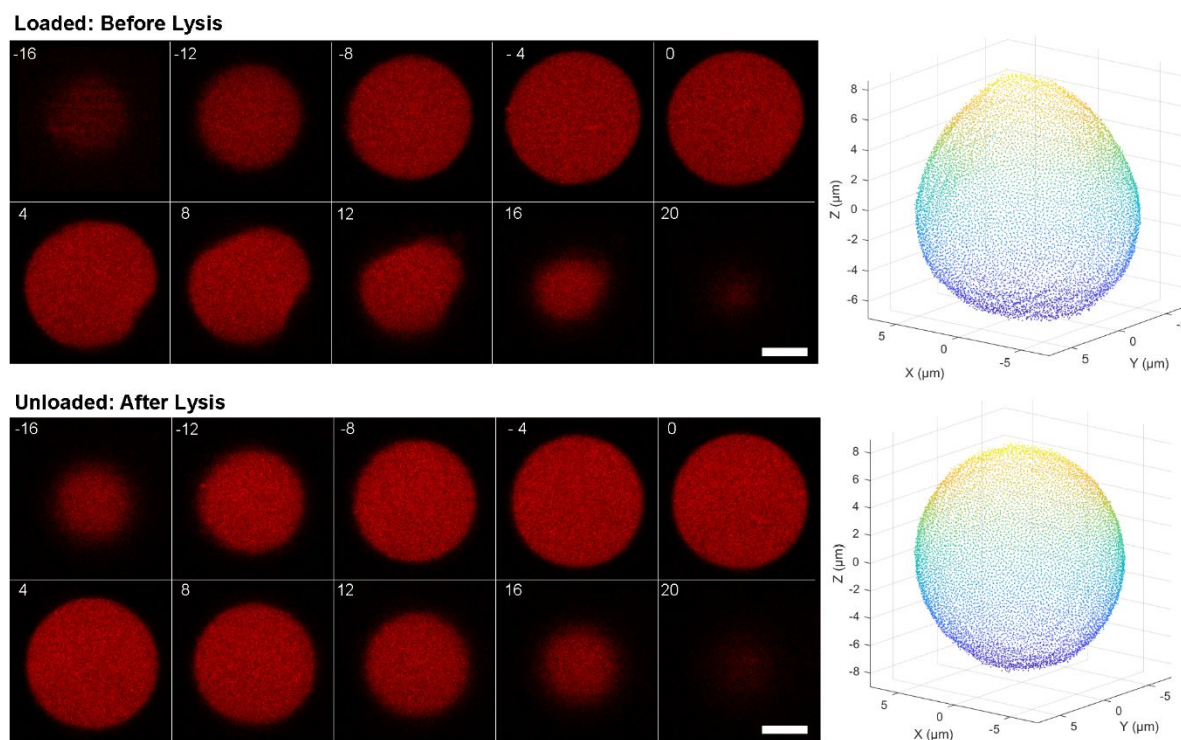

Figure 2: At left, thumbnail images show *z*-slices taken from the three-dimensional confocal image stack of a μTFM PEG-based microsphere sensor before lysis (cell-loaded) at top, and after lysis (unloaded) at bottom. In each image, the red dye volumetrically labels the hydrogel. The scale bar represents 5 μm in both image sets. The small numbers in the upper left corners indicate the slice number, where a slice number of 0 represents the approximate center of the sphere along the *z*-axis. The physical distance between each image shown is 1.6 μm (the distance between each *z*-plane is 0.4 μm). At right, a 3D scatterplot of the surface coordinates (a 'pointcloud'), determined from fitting the 1D intensity profile along each ray is shown. Here 10,000 points are shown from a PLL-coated microsphere. The colormap indicates *z*-location and is used for display purposes only.

2.3 Formulism for Traction Calculation

In the unloaded state, the sensor was spherical and we assumed that its initial radius is $R = \sum_{i=1}^{N} |x^{(i)}|$ /N, where $x^{(i)} = \{x_1^{(i)}, x_2^{(i)}, x_3^{(i)}\}$ denotes the location of the i-th material point along the surface of the unloaded sensor. Typically, R was $\sim 10 \, \mu m$, comparable to the cell size. When we placed the sensors within small multicellular aggregates, we observed that the sensors experienced small strains and volumetric deformations under loading by adjacent cells, and as a result became compressed and roughly ellipsoidal.

In order to compute the tractions that the cells exert on the sensors, we must first determine the mapping of the material points along the surface of the sensor from the initial to the deformed state. We emphasize that this mapping is not unique since multiple displacements can lead to the deformed state [24]. Based on the experimental observations, we decomposed the deformation of the sensors into two stages, as described in the following, and determined the mapping of the material points along the surface of the sensor from the unloaded to the cell-loaded states accordingly.

In the first stage, we assumed the homogeneous deformation of the microsphere into an ellipsoid whose surface was determined from a least-squares fit of the discretized points along the surface of the cell-loaded configuration. A fit of 8 data sets revealed that the deviations of the cell-loaded state from an ellipsoidal-shape $d_{el} < 0.4 \, \mu m$, where $d_{el} = \sqrt{\frac{1}{N}\sum_{i=1}^{N} |y^{(i)} - y_{el}^{(i)}|^2}$ and $y^{(i)}$ and $y_{el}^{(i)}$ denote the i-th material point along the surface of the cell-loaded sensor and the ellipsoidal approximation, respectively. To better understand the tractions that the cells exert within the multicellular aggregate, we computed the ratio between the maximum and the minimum axes of the ellipsoid $\xi \geq 1$, where $\xi = 1$ refers to a sphere that experiences an isotropic stress state and remains spherical. Empirically, we found $1.03 \leq \xi \leq 1.065$ in 7 data sets and $\xi \approx 1.16$ in the 8th, while the volumetric deformations $\Delta V/V$ ranged from -0.10 to -0.07.

Since the deviations of the deformed sensor shape from the ellipsoidal shape are small, we next assumed that the material points along the surface of the measured ellipsoid displace radially to recover the cell-loaded state. This simplifying assumption is based on the experimental observations and significantly reduces computational complexity and cost. The small radial displacements account for the inhomogeneities that arise from the slightly asymmetric force distribution resulting from the cells around the sensor. However, the framework presented in the following is general, and other displacement boundary conditions could certainly be chosen to fit different cases as needed. For cases where high-resolution measurements of shear tractions are desired, particle-based tracking methods that enable the full 3D deformation field to be uniquely determined are recommended, as the boundary-based tracking used here is insensitive to in-plane displacements, albeit at the expense of significantly more image processing steps.

The total displacement of the i-th material point from the unloaded to the cell-loaded configuration was obtained by the summation of the displacements from the two steps and is denoted by $u_m^{(i)}(x^{(i)}) = y^{(i)}(x^{(i)}) - x^{(i)}$.

Having mapped the displacements of a discrete number of points along the surface of the sensor from the unloaded to the cell-loaded states, our next goal is to find an appropriate continuous displacement field that satisfies equilibrium and maps all of the material points from the reference to the deformed shape of

the sensor. Once the displacement field is obtained, the tractions can be easily computed via Hooke's law. To this end, we employed the Papkovich-Neuber solution to the linear elastic problem.

First, we consider a body occupying a volume Ω with a boundary $\partial\Omega$ and material points that are denoted by $\boldsymbol{x} = \{x_1, x_2, x_3\}$. As a result of an external loading due to the actions of the neighboring cells within the aggregate, the material points experience the displacement field $\boldsymbol{u}_{eq}(\boldsymbol{x})$. The equilibrium equation can be written in terms of the displacement field $\boldsymbol{u}_{eq}$

$$\left(\frac{K}{G'} + \frac{1}{3}\right)\nabla\nabla \cdot \boldsymbol{u}_{eq} + \nabla \cdot \nabla\boldsymbol{u}_{eq} = 0. \tag{1}$$

The general solution to Eq. (1) for the equilibrium displacement field can be written in terms of harmonic potential functions

$$\boldsymbol{u}_{eq} = \frac{8G' + 6K}{G' + 3K}\boldsymbol{\psi} - \nabla(\boldsymbol{x} \cdot \boldsymbol{\psi} + \chi), \tag{2}$$

where $\boldsymbol{\psi} = \{\psi_1, \psi_2, \psi_3\}$ is a harmonic potential vector, χ is a harmonic scalar potential that we set to zero, and we neglect body forces.

In Cartesian coordinates, the three components of the potential vector $\boldsymbol{\psi}$ are expressed in terms of a summation of spherical harmonic functions of order m and degree l that can be written as $Y_{lm} = \Pi_{lm}A_m$, where

$$\Pi_{lm} = \sqrt{\frac{(l-m)!}{(l+m)!}} \sum_{k=0}^{\frac{l-m}{2}} (-1)^k 2^{-l} \frac{(2(l-k))!}{k!(l-k)!(l-2k-m)!} r^{2k} x_1^{l-2k-m}, \tag{3}$$

$$r = \sqrt{x_1^2 + x_2^2 + x_3^2}, \text{ and}$$

$$A_m = \sum_{k=0}^{m} \frac{m!}{k!(m-k)!} x_2^k x_3^{m-k} \begin{cases} \cos\left((m-k)\frac{\pi}{2}\right) & 0 \leq m \leq l \\ \sin\left((m-k)\frac{\pi}{2}\right) & -l \leq m < 0 \end{cases}.$$

Accordingly, the i-th component of the potential vector can be written as the summation

$$\psi_i = \sum_{j=0}^{l}\sum_{m=-j}^{j} c_{jm}^{(i)} Y_{jm}, \tag{4}$$

where $c_{jm}^{(i)}$ is a coefficient of order m and degree j that multiplies the spherical harmonic function Y_{jm}, and l determines the degree of the harmonic potential vector $\boldsymbol{\psi}$.

Using the measured reference (unloaded) and the deformed (loaded) shapes of the sensor, we aim to

find a displacement field $\boldsymbol{u}_{eq}$ (Eq. 2) that maps the material points accordingly between the two shapes. To this end, we employ the least-squares regression method to fit the unknown coefficients $c_{jm}^{(i)}$ of the equilibrium displacement field $\boldsymbol{u}_{eq}$ to the displacements $\boldsymbol{u}_m^{(i)}$ of the measured discretized points along the surface of the deformed gel sensor. The degree of the spherical harmonics function l determines the accuracy of the fit, with higher values of l leading to better approximations but also longer computational times. We caution that taking values of l that are too high may also capture experimental noise rather than physical phenomena.

In order to fit the displacements of the discretized points along the surface of the microsphere to the equilibrium displacement solution, it is convenient to write $\boldsymbol{\psi} = \boldsymbol{Y}\,\boldsymbol{C}$ where $\boldsymbol{Y}$ is a 3 x n matrix containing the spherical harmonic functions Y_{lm} and $\boldsymbol{C}$ is an n x 1 vector containing the unknown coefficients $c_{jm}^{(i)}$. The number of unknown coefficients is directly related to the polynomial degree l via $n = 3\sum_{i\,=\,0}^{l}(1 + 2\,i)$. Thus, we can write the equilibrium displacement field as

$$\boldsymbol{u}_{eq}(\boldsymbol{x},l) = \boldsymbol{M}(\boldsymbol{x},l)\,\boldsymbol{C}, \tag{5}$$

where $\boldsymbol{M} = \dfrac{8G' + 6K}{G' + 3K}\boldsymbol{Y} - \nabla(\boldsymbol{x}\,\boldsymbol{Y})$ is a 3 x n matrix. This formulation can be easily used to fit to the experimentally measured displacements in order to determine the best-fit coefficient vector $\boldsymbol{C}$. In the limit of negligible experimental uncertainty, this approach provides the exact solution for spheres that deform into ellipsoids under homogeneous deformations.

Once the equilibrium displacement field has been computed, we can easily determine the strain $\boldsymbol{\varepsilon}(\boldsymbol{x}) = (\nabla\boldsymbol{u}_{eq} + \nabla\boldsymbol{u}_{eq}^T)/2$ and use Hooke's law $\boldsymbol{\sigma}(\boldsymbol{x}) = 2G\,\boldsymbol{\varepsilon}(\boldsymbol{x}) + (K - 2G/3)\,\mathrm{Tr}(\boldsymbol{\varepsilon}(\boldsymbol{x}))\,\mathbf{I}$ to calculate the stress. Consequently, the tractions along the surface of the sensor are given by $\boldsymbol{t}(\boldsymbol{x}) = \boldsymbol{\sigma}(\boldsymbol{x})\cdot\hat{\boldsymbol{n}}$, where $\hat{\boldsymbol{n}}$ is the normal pointing away from the surface at point $\boldsymbol{x}$. This allows estimation of the normal and the shear tractions $t_n = \boldsymbol{t}\cdot\hat{\boldsymbol{n}}$ and $t_s = \sqrt{\boldsymbol{t}\cdot\boldsymbol{t} - t_n^2}$, respectively, exerted collectively by the cells upon the sensor.

In solving this inverse problem, we understand that the mapping function is not necessarily unique since there may be multiple displacement fields that result in the deformed boundary. In principle, volumetric boundary tracking could help constrain this degeneracy and provide a more unique solution, although in practice such mapping would likely require small incremental displacements to be recorded over time to ensure that particle identity is uniquely retained as the volume deformed.

In this analysis, we have limited our treatment to the linear deformation regime of the microparticle sensors. In practice, it should be possible to tune the sensor mechanics to remain within this limit for most systems of study. In the event that softer sensors are required to access specific mechanobiological responses or biological regimes, it is in principle possible to extend the analysis presented here to consider nonlinear mechanical models, as recently described [25-27].

2.4 Experimental Validation

To validate this approach to traction determination, we embedded the compressible microsphere sensors into aggregates of mouse 3T3 fibroblast cells, measured the sensor shape under loading and after lysis (unloaded) and calculated the tractions, as described above. Representative normal traction maps calculated from the deformation of microsphere sensors embedded in are shown in Fig. 3. The normal

tractions were in the range of kPa for both PLL- and RGD-coated microspheres, and the calculated shear tractions were significantly smaller ($\sim$ 10s of Pa), as expected based on the volumetric compression of the sensors into ellipsoids and the fact that $K \gg G'$ for these sensors (Supplementary Fig. S1). Normal tractions were also found to dominate in a recent FE-based μTFM study of melanoma cell aggregates [9]. We did not observe significant differences using PLL- or RGD-coated microsphere sensors respectively.

(e)		PLL 1	PLL 2	RGD 1	RGD 2
$\langle t_n \rangle$	(kPa)	−1.44	−0.98	−1.47	−1.2
$\lvert t_n \rvert^{min}$	(kPa)	1.32	0.71	1.4	1.09
$\lvert t_n \rvert^{max}$	(kPa)	1.58	1.3	1.6	1.4
SD	(kPa)	0.04	0.08	0.03	0.05
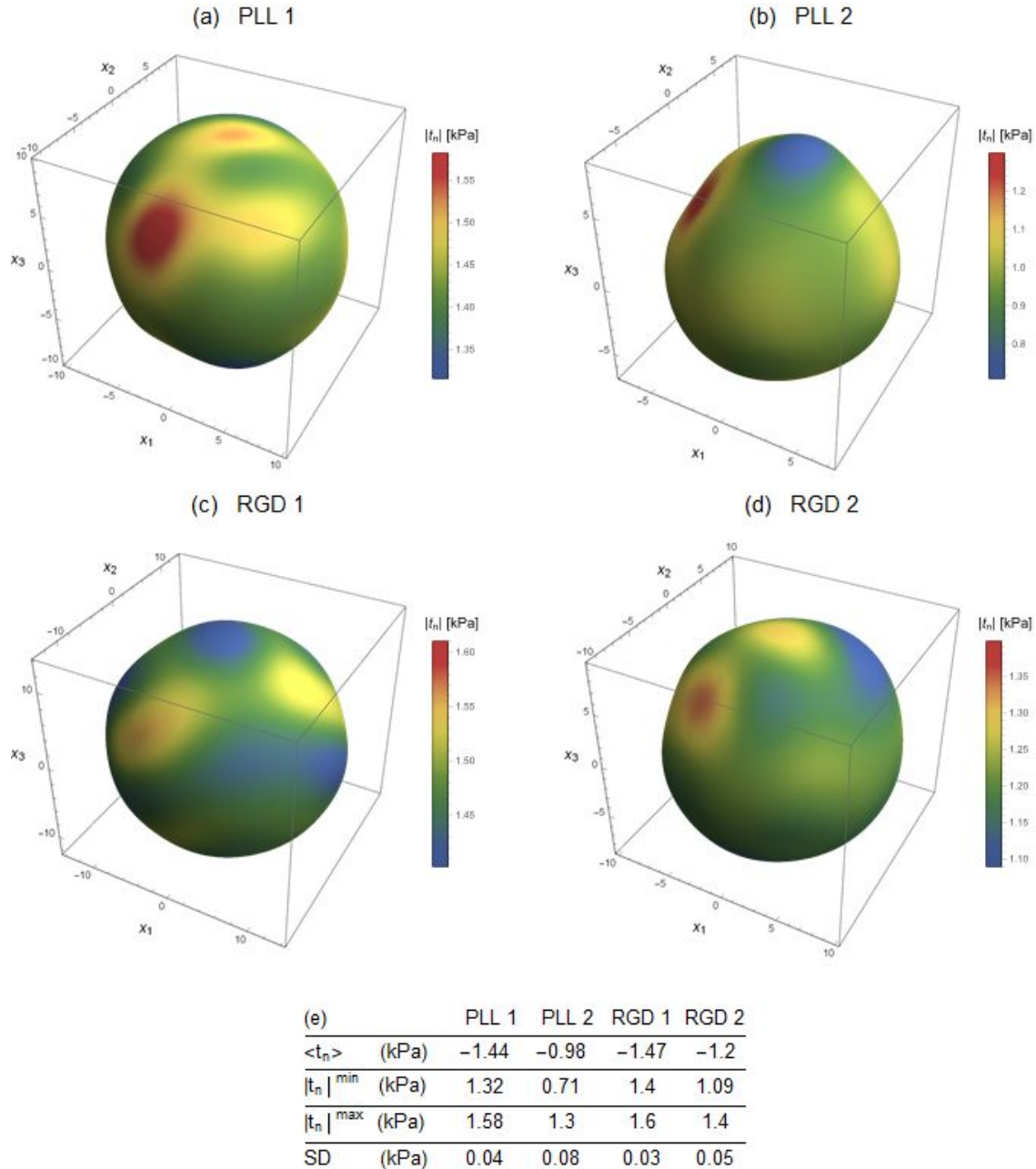
Figure 3. Normal tractions for **(a,b)** PLL-coated and **(c,d)** RGD-coated microspheres, respectively, embedded in 3T3 fibroblast aggregates. **(e,f)** Table of mean traction force values, as well as the extremal traction magnitudes and the standard deviations for each sensor shown.

This may be due to reduced focal adhesion complex maturation on RGD-coated hydrogel microspheres, as previously observed [9], in contrast to 2D culture results [28] or, it may indicate that the fibroblasts have secreted enough extracellular matrix proteins to permit integrin functionality on the PLL–coated spheres. Alternatively, the surface functionalization could promote transmission of actomyosin contraction forces that are not focal-adhesion dependent.

The efficient computational approach presented here is significantly easier to implement than FE methods or bead tracking. For a typical image volume of 10-30 μm size, with 2000 discretized surface points, surface reconstruction takes < 5 minutes, and the full 3D traction field can be estimated in < 10 minutes for $l \leq 6$. With $l = 6$, we measured an average local computational error $d = \sqrt{\frac{1}{N}\Sigma_{i=1}^{N}|y^{(i)}(x^{(i)}) - y_{eq}(x^{(i)},l)|^2}$ of approximately $0.12 - 0.18\,\mu m$. A significant improvement in the approximation was observed as l was increased from 1 to 6 (Fig. 4). Whereas for $l = 7$ or 8, the computation time increased over ten-fold to ~2 hours, while only slightly reducing $d \sim 0.10 - 0.17\,\mu m$. These values approach our estimated experimental error in surface determination, $\sim \pm\,0.1\,\mu m$, suggesting that our approximation is approaching maximum computational accuracy.
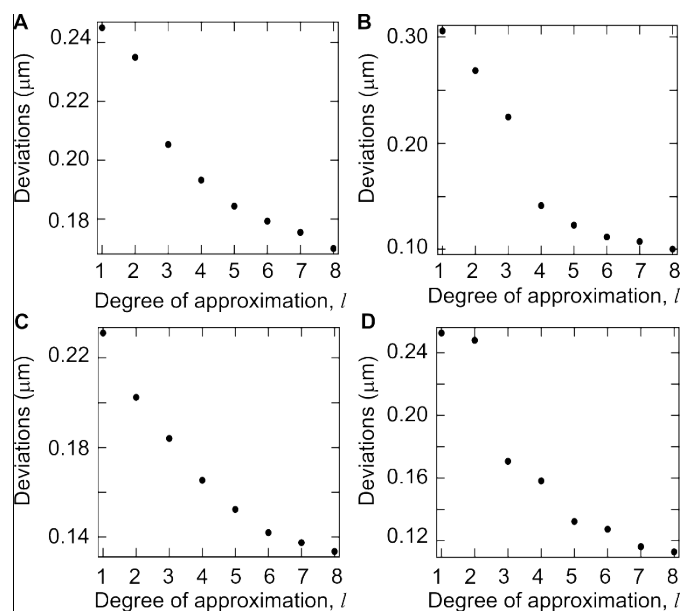

Figure 4: The deviations as a function of the degree of approximation *l* for the (**a**,**b**) PLL-coated and (**c**,**d**) RGD-coated microspheres shown. Normal and shear tractions are presented in Figure 3 and Figure S1, respectively.

During the revision of this manuscript, a complementary approach to μTFM that uses a cost function minimization approach was demonstrated to measure the tractions exerted during phagocytic engulfment [24]. However, minimizing the cost function is extremely time intensive, leading to high computational costs for this approach. Our method, which is based on the experimental observations of sensors embedded within multicellular aggregates, allows rapid determination of the tractions.

3. Conclusions

We presented a new approach to measuring cell-generated forces from the deformations of elastic microspheres embedded within multicellular aggregates, which are difficult to investigate with classic TFM methods. The significant increase in computational speed reported here not only enables faster data analysis, but opens the door to nearly simultaneous analysis of images and tractions during image acquisition. Access to such real-time information could enable immediate feedback between experiment and analysis, ultimately resulting in the measurement of dynamic properties of time-evolving multicellular systems *in situ.*

Author Contributions

BK and MTV conceived and initiated the project. AHK, BK and MTV designed experiments. BK developed the image analysis and surface reconstruction routines and initiated the computational work. NC developed the mathematical framework and the computational analysis. AHK manufactured the microspheres and performed all experiments. All authors analyzed data. AHK, NC, and MTV wrote, and all authors edited, the manuscript.

Conflicts of Interest

There are no conflicts to declare.

References

1. C. Franck, S. A. Maskarinec, D. A. Tirrell and G. Ravichandran, *PLOS ONE*, 2011, **6**, e17833.
2. V. Maruthamuthu, B. Sabass, U. S. Schwarz and M. L. Gardel, *Proceedings of the National Academy of Sciences*, 2011.
3. X. Wang and T. Ha, *Science*, 2013, **340**, 991.
4. N. Gjorevski, A. S. Piotrowski, V. D. Varner and C. M. Nelson, *Scientific Reports*, 2015, **5**, 11458.
5. S. Khetan, M. Guvendiren, W. R. Legant, D. M. Cohen, C. S. Chen and J. A. Burdick, *Nature Materials*, 2013, **12**, 458.

6. S. J. Streichan, C. R. Hoerner, T. Schneidt, D. Holzer and L. Hufnagel, *Proceedings of the National Academy of Sciences*, 2014, **111**, 5586.

7. M. E. Dolega, M. Delarue, F. Ingremeau, J. Prost, A. Delon and G. Cappello, *Nature Communications*, 2017, **8**, 14056.

8. F. Ingremeau, M. E. Dolega, J. Gallagher, I. Wang, G. Cappello and A. Delon, *Soft Matter*, 2017, **13**, 4210-4213.

9. E. Mohagheghian, J. Luo, J. Chen, G. Chaudhary, J. Chen, J. Sun, R. H. Ewoldt and N. Wang, *Nature Communications*, 2018, **9**, 1878.

10. W. Lee, N. Kalashnikov, S. Mok, R. Halaoui, E. Kuzmin, A. J. Putnam, S. Takayama, M. Park, L. McCaffrey, R. Zhao, R. L. Leask and C. Moraes, *Nature Communications*, 2019, **10**, 144.

11. W. R. Legant, J. S. Miller, B. L. Blakely, D. M. Cohen, G. M. Genin and C. S. Chen, *Nature Methods*, 2010, **7**, 969.

12. J. Steinwachs, C. Metzner, K. Skodzek, N. Lang, I. Thievessen, C. Mark, S. Münster, K. E. Aifantis and B. Fabry, *Nature Methods*, 2015, **13**, 171.

13. M. S. Hall, R. Long, X. Feng, Y. Huang, C.-Y. Hui and M. Wu, *Experimental Cell Research*, 2013, **319**, 2396-2408.

14. O. Campàs, T. Mammoto, S. Hasso, R. A. Sperling, D. O'Connell, A. G. Bischof, R. Maas, D. A. Weitz, L. Mahadevan and D. E. Ingber, *Nature Methods*, 2013, **11**, 183.

15. F. Serwane, A. Mongera, P. Rowghanian, D. A. Kealhofer, A. A. Lucio, Z. M. Hockenbery and O. Campàs, *Nature Methods*, 2016, **14**, 181.

16. N. R. Labriola, J. S. Sadick, J. R. Morgan, E. Mathiowitz and E. M. Darling, *Annals of Biomedical Engineering*, 2018, **46**, 1146-1159.

17. S. Girardo, N. Träber, K. Wagner, G. Cojoc, C. Herold, R. Goswami, R. Schlüßer, S. Abuhattum, A. Taubenberger, F. Reichel, D. Mokbel, M. Herbig, M. Schürmann, P. Müller, T. Heida, A. Jacobi, E. Ulbricht, J. Thiele, C. Werner and J. Guck, *Journal of Materials Chemistry B*, 2018, **6**, 6245-6261.

18. A. A. D'souza and R. Shegokar, *Expert Opinion on Drug Delivery*, 2016, **13**, 1257-1275.

19. E. Bakaic, N. M. B. Smeets and T. Hoare, *RSC Advances*, 2015, **5**, 35469-35486.

20. A. Cavallo, M. Madaghiele, U. Masullo, M. G. Lionetto and A. Sannino, *Journal of Applied Polymer Science*, 2017, **134**.

21. S. Monnier, M. Delarue, B. Brunel, M. E. Dolega, A. Delon and G. Cappello, *Methods*, 2016, **94**, 114-119.

22. C. Bonnet-Gonnet, L. Belloni and B. Cabane, *Langmuir*, 1994, **10**, 4012-4021.

23. Y. Hu, X. Zhao, J. J. Vlassak and Z. Suo, *Applied Physics Letters*, 2010, **96**, 121904.

24. D. Vorselen, Y. Wang, M. M. de Jesus, P. K. Shah, M. J. Footer, M. Huse, W. Cai and J. A. Theriot, *Nature Communications*, 2020, **11**, 20.

25. L. Dong and A. A. Oberai, *Computer Methods in Applied Mechanics and Engineering*, 2017, **314**, 296-313.

26. N. Cohen, *International Journal of Solids and Structures*, 2019, **178-179**, 81-90.

27. N. Cohen and R. M. McMeeking, *Journal of the Mechanics and Physics of Solids*, 2019, **125**, 666-680.

28. V. Swaminathan, J. M. Kalappurakkal, S. B. Mehta, P. Nordenfelt, T. I. Moore, N. Koga, D. A. Baker, R. Oldenbourg, T. Tani, S. Mayor, T. A. Springer and C. M. Waterman, *Proceedings of the National Academy of Sciences*, 2017, **114**, 10648-10653.

GRAPHICAL ABSTRACT

We measure cell-generated forces from the deformations of elastic microspheres embedded within multicellular aggregates. By directly fitting the measured sensor deformation to an analytical model, we dramatically reduce the computational complexity of the problem, and directly obtain the full 3D mapping of surface stresses within minutes.